PCCP

The effect of grain size on the hydration of BaZr0.9Y0.1O3-δ proton conductor studied by ambient pressure X-ray photoelectron spectroscopy

Journal:	*Physical Chemistry Chemical Physics*
Manuscript ID	CP-ART-08-2019-004335.R1
Article Type:	Paper
Date Submitted by the Author:	09-Jul-2019
Complete List of Authors:	Jarry, Angelique; University of Maryland at College Park, Materials Science and Engineering; University of Maryland at College Park, Chemistry and Biochemistry Jackson, Gregory; Colorado School of Mines, Department of Mechanical Engineering Crumlin, Ethan; Lawrence Berkeley National Laboratory, Advanced Light Srouce Eichhorn, Bryan; University of Maryland, Department of Chemistry Ricote, Sandrine; Colorado School of Mines, Department of Mechanical Engineering

SCHOLARONE™
Manuscripts

The effect of grain size on the hydration of $BaZr_{0.9}Y_{0.1}O_{3-\delta}$ proton conductor studied by ambient pressure X-ray photoelectron spectroscopy

Angelique Jarry[1,2,*], Gregory S. Jackson[3], Ethan J. Crumlin[4], Bryan Eichhorn[2], Sandrine Ricote[3,*]

1 Materials Science and Engineering, University of Maryland, College Park, MD 20742, USA

2 Chemistry and Biochemistry, University of Maryland, College Park, MD 20742, USA

3 Department of Mechanical Engineering, Colorado School of Mines, Golden, CO 80401, USA

4 Advanced Light Source, Lawrence Berkeley National Laboratories, Berkeley, CA 94720, USA

Corresponding authors: ajarry@umd.edu; sricote@mines.edu

Abstract:

Three $BaZr_{0.9}Y_{0.1}O_{3-\delta}$ (BZY10) pellets were prepared using different sintering processes, resulting in samples with different grain sizes, from 0.3 to 5 microns. Ambient pressure X-ray photoelectron spectra were recorded in argon, steam and oxygen atmospheres (100 mTorr) in the 300-500 °C temperature range. Deconvolution of O 1s peaks reveals 4 distinct contributions: sub-surface lattice oxide, termination layer oxides, OH^- and gas-phase steam in wet environments. The OH^- contribution of the O 1s peak includes sub-surface incorporation of protonic defects in the lattice related to hydration as well as surface hydroxylation and molecular water adsorption. The OH^- concentration increases with grain size and with decreasing the analysis depth. These results suggest that grain boundaries associated with the larger grains adsorbed water more effectively. Thus, larger grains, which increase proton conductivity in BZY10, may also enhance catalytic activity for carbonaceous fuel oxidation by facilitating increased hydration and surface carbon removal.

Keyword: yttrium-doped barium zirconate, proton-conductor, AP-XPS, hydration, grain size

1. Introduction:

Yttrium-doped barium zirconate ($BaZr_{1-x}Y_xO_{3-\delta}$, BZY) is one of the most studied high-temperature proton-conductors[1,2,3,4]. BZY perovskites exhibit mixed conductivity, with predominantly electronic conduction in oxidizing atmosphere and predominantly ionic (protonic defect and oxygen vacancy) conduction at lower oxygen partial pressures (P_{O2}) below 10^{-6} atm [5,6,7,8]. Isotope exchange measurements[9] and electromotive force measurements (EMF)[10] have distinguished the protonic defect contribution from the oxygen vacancy contribution of the total conductivity. Up to 600 °C BZY ionic conductivity is dominated by proton conduction, with only 1.5 and 4.5 % of oxide ion conduction at 600 °C for $BaZr_{0.9}Y_{0.1}O_{3-\delta}$ (BZY10) and $BaZr_{0.8}Y_{0.2}O_{3-\delta}$ (BZY20) respectively [10].

Protonic defects ($OH_O^{\bullet}$) are incorporated into high-temperature proton-conducting materials according to the Stotz-Wagner hydration reaction (R1) [11,12,13], which is exothermic with $\triangle H° \approx$ -80 kJ·mol^{-1} [1,7,14,15]. Figure 1 illustrates how surface vacancies $V_O^{\bullet\bullet}$ provide a site for dissociative H_2O adsorption and incorporation of $OH_O^{\bullet}$ into the near surface lattice.

$$H_2O(g) + V_O^{\bullet\bullet} + O_O^x \leftrightarrow 2OH_O^{\bullet} \qquad \text{(R1)}$$

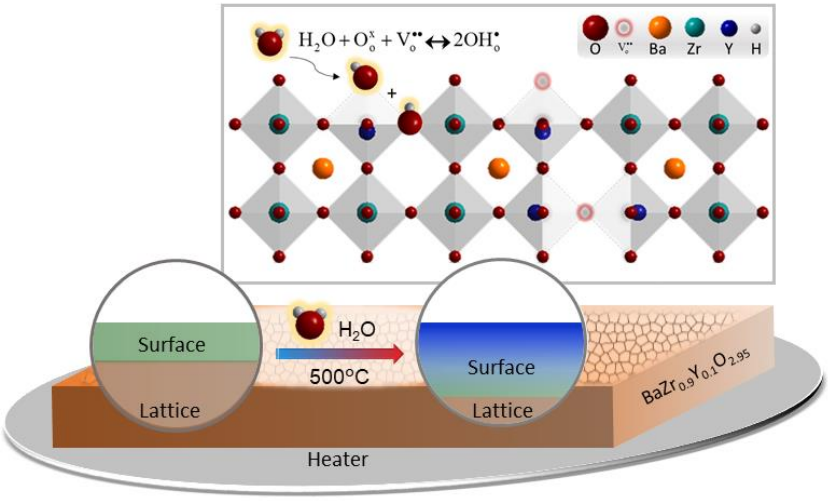

Figure 1: Illustration of the Stotz-Wagner hydration reaction, which shows proton-defect incorporation into the BZY10 lattice.

In support of conductivity measurements, the presence of bulk protonic defects can be determined by thermogravimetric measurements[1,7,15,16,17], high temperature X-ray diffraction

[18,19,20,21], proton-NMR [22], hydrogen probe [23], and Raman profilometry [24]. While all the former techniques provide bulk measurements, ambient-pressure X-ray photoelectron spectroscopy (AP-XPS)[25,26] offers the unique opportunity to observe surface and near-surface chemistry, up to tens of nanometers [26,27], during hydration of the high-temperature proton conductors. Furthermore, modulating the X-ray source photon energy can allow depth profiling near the surface to assess variation in interfacial chemistry as a function of depth. Our group has successfully used AP-XPS to investigate composition effect on surface chemistry of epitaxial thin films of $BaCe_xZr_{0.9-x}Y_{0.1}O_{3-\delta}$ (x = 0; 0.2; 0.9) perovskites.[26] These hydration studies of BZY10 thin film led to the following conclusions [26]:

- Major changes upon hydration were only observed in the O 1s and Y 3d core-level spectra.
- Hydration is associated with surface secondary phase growth with oxygen under coordinated yttrium and/or yttrium hydroxide.
- The presence of sulfur (common contaminant in $BaCO_3$) in high-temperature oxidative environments leads to the formation of surface SO_4^{2-}, which rapidly desorbs from the BZY10 surface.

Measured values of protonic conductivity in BZY10 materials varies over 2 order of magnitudes (~10^{-5} to ~10^{-3} S cm^{-1} at 400 °C) [2], and this wide variation in conductivities was explained by differences in ceramic processing leading to (i) barium non-stoichiometry [28,29], (ii) increased disorder in the grain-boundary region [30], (iii) presence of impurity or dopant segregation at the grain-boundaries [31,32,33,34], (iv) cross substitution of yttrium on the A-site[35], and (v) intrinsic positive charge at the grain boundary due to preferential oxygen segregation and associated proton depletion in the space charged layers [36,37,38,39,40,41].

In this work, three $BaZr_{0.9}Y_{0.1}O_{3-\delta}$ (BZY10) specimens were prepared with different ceramic processing techniques and investigated by AP-XPS to correlate the extent of hydration to grain microstructure. O 1s peaks are deconvoluted into four contributions, including one peak (with the second to the highest binding energy) corresponding to surface hydroxylation and adsorbed molecular water (designated OH^-). This contribution appeared under humid conditions and its importance was analyzed as a function of temperature and analysis depth to reveal significant insights into how grain structure and operating conditions impact BZY10 surface activity.

2. Experimental:

The three BZY10 samples were prepared as followed:

- spark plasma sintering: 5 min at 1700 °C (SPS) [41],
- solid-state reaction without sintering aid, sintered at 1700 °C for 24h (SSR) [7],
- solid-state reaction without sintering aid, conventionally sintered at 1720 °C and annealed at high temperature 2200 °C (HT) [42].

The information about the precursors used for the synthesis, as well as the obtained XRD patterns are summarized in Table 1 and Figure 1 of the Supplementary Information.

In this study, none of the BZY10 samples contain sintering aids such as Ni. The microstructure of the three samples is reported in detail elsewhere [7,42,43] and summarized below in the results section.

AP-XPS spectra at elevated sample temperatures were collected at Beamline 9.3.2 at Lawrence Berkeley National Laboratory's (LBNL) Advanced Light Source (ALS) [44]. BZY10 pellets were held by spring-loaded tips onto an Al_2O_3 plate heater. A thermocouple onto the sample surface, as illustrated in Figure 2, provided a control temperature for the heater power. The surface of the samples was cleaned with a pretreatment at 500 °C under ultra-high vacuum (UHV) to remove adventitious carbon and to dehydrate the sample.

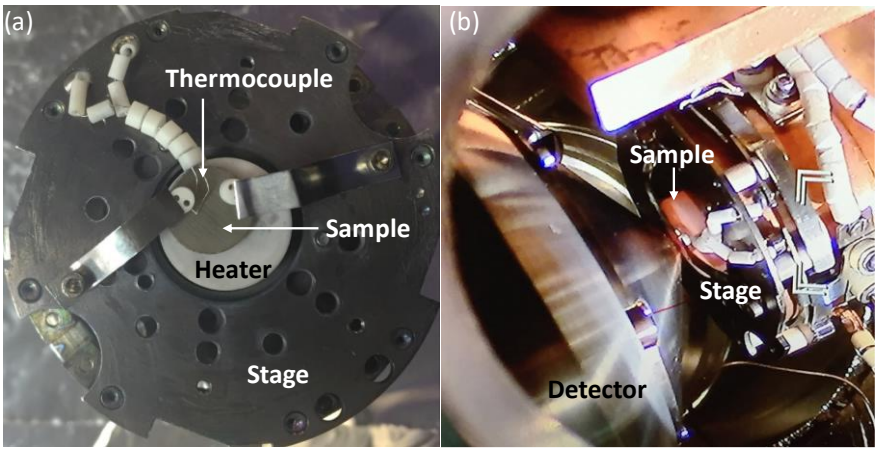

Figure 2: SSR BZY10 sample on the sample holder (a) outside and (b) inside the AP-XPS chamber.

AP-XPS spectra were recorded at T = 300 °C and 500 °C in the following gas conditions: 100 mTorr of Ar, 100 mTorr H_2O, and 100 mTorr O_2. Different XPS source excitation beam energies, within the range of Beamline 9.3.2 (800 eV, 710 eV, 630 eV, 490 eV and 300 eV), were used to explore a range of near-surface depths with a spot-size of ~ 0.8 mm (allowing for a statistical number of grains and grain boundaries). Table 1 summarizes the different core-electron spectra recorded for each condition. The sample was heated at about 5 °C/min to the test temperature and held at constant T for 20 min before collecting XPS spectra. Spectra were fitted in Casa-XPS software (Casa Software Ltd., UK, http://www.casaxps.com/) using a combined Gaussian-Lorentzian line shape and a Shirley background. Similarly to our previous work [26], the Ba 4d peak of barium perovskite at 88.9 eV was used for calibration. Spectra fitting and normalization are described in detail elsewhere.[26]

Table 1: Collection of spectra for one gas composition/temperature condition:

Beam energy (eV)	Low resolution survey spectrum	High resolution spectra
300 eV	0-150 eV	Ba 4d
490 eV	0-390 eV	C 1s, Ba 4d, Y 3d, Zr 3d
630 eV	0-600 eV	O 1s, Ba 4d
710 eV	0-600 eV	O 1s, C 1s, Ba 4d, Y3d, Zr 3d
800 eV	0-700 eV	O 1s, C 1s, Ba 4d, Y 3d, Zr 3d

Greater analysis depths can be obtained at higher beam energies. Figure 3 represents a perovskite structure with the analysis depth for the different elements as a function of the beam energy. The stoichiometry was determined as already explained in reference [26] (supplementary information: page S2). Beam energies were chosen to provide at least three different inelastic mean free paths (IMFP, i.e., measurement depths) for each element.

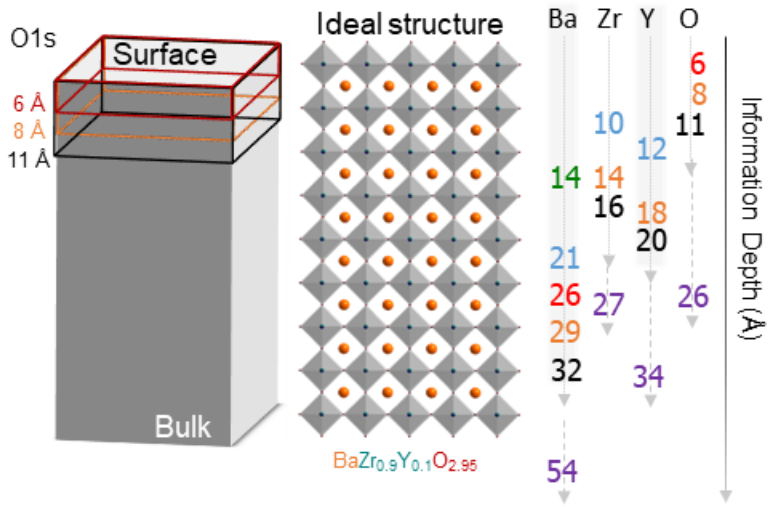

Figure 3: Inelastic mean free path (IMFP) values in Angstrom (A) calculated with Tanuma, Powell, Penn formula (TPP-2M [26]) for Ba 4d, Zr 3d, Y 3d and O 1s with incident photon energy of 300 eV (green), 490 eV (blue), 630 eV (red), 710 eV (orange), 800 eV (black) and 1487 eV (purple). Higher beam energies can obtain useful distinctive signal for each elements at higher depths normal to the surface, and comparison of spectra at different energies provides information of near-surface chemistry information as a function of depth.

3. Results:

3.1. Microstructural and chemical characterizations of the samples

The grain size ranges from 0.3-0.8 microns, ≈1 micron, ≈ 2-5 microns for the SPS, SSR and HT samples respectively as illustrated in Figure 4. It is important to note that the microstructures for the SPS and SSR samples were observed on thermally etched surfaces and that the surfaces of the samples were polished before the AP-XPS measurements.

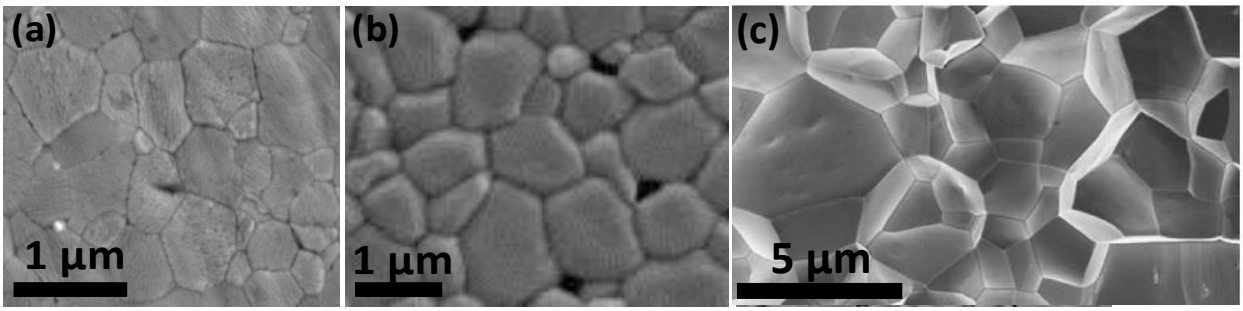

Figure 4: Secondary electron micrographs of the thermally etched surfaces of the samples (a) SPS [43], (b) SSR and (c) fractured cross section the HT sample [42] (by permission of Elsevier LDT).

The conductivity and chemical compositions have been previously studied for the SPS and HT samples [43,45]. Both samples exhibited similar bulk conductivity in 3% moist 5 % H_2 [43]. The bulk and grain boundary chemical compositions were also determined by atom–probe tomography [45]. Both samples exhibited barium and yttrium segregation and an associated slight depletion of zirconium and oxygen at the grain boundaries. It is important to note that secondary phases such as barium oxide and yttrium oxide may be present at the grain-boundaries. The ratio for Ba, Zr, Y and O between the grain boundaries and the bulk are summarized in Table 2.

Table 2: Comparison of the chemical composition determined by atom probe tomography for the SPS and HT samples (average on three grain boundaries) [45]. The ratio of the grain boundary concentration over the bulk concentration is reported for Ba, Zr, Y and O. A value of 1 represents a similar composition for the bulk and the grain boundaries, while values > 1 refer to a segregation to the grain boundaries.

	$[Ba]_{GB}/[Ba]_{bulk}$	$[Zr]_{GB}/[Zr]_{bulk}$	$[Y]_{GB}/[Y]_{bulk}$	$[O]_{GB}/[O]_{bulk}$
HT sample	1.25 (±0.03)	0.98 (±0.01)	1.18 (±0.04)	0.97 (±0.01)
SPS sample	1.15 (±0.02)	0.97 (±0.01)	1.20 (±0.04)	0.98 (±0.01)

3.2. AP-XPS results

3.2.1. Survey spectra after surface cleaning

Sample survey spectra at 710 eV, 500 °C in 100 mTorr Ar after cleaning at 500 °C under UHV for the three samples are given in Figure 5. The calibration on the Ba 4d peak is necessary to correct for charging effects, which vary with temperature and gas atmosphere. The absence of C 1s peak at 284-288 eV (Figure 2 SI) confirms that the cleaning removes all the adventitious carbon and carbonate species at the surface of the samples.

Several impurities are visible on the survey spectra:

- Sulphur (161-169 eV): very little amounts are detected for the three samples and the contribution disappears at temperature under oxidative environment (desorption of SO_4^{2-}). This trend is very similar to what was observed on BZY thin films [26].

- Silicon (152-154 eV): The surface of the samples was polished with SiC discs. Silicon is also a common impurity in zirconia.
- Molybdenum: The doublet in the 228-233 eV energy range corresponds to the Mo 3d peaks. This impurity segregates to the surface of the samples at temperature.

These impurity peaks do not interfere with the spectral analysis of the important O 1s and Y 3d peaks. Although their presence may impact the surface chemistry to some extent, similar impurity amounts for the three samples suggests that these effects are relatively similar for all the tests.

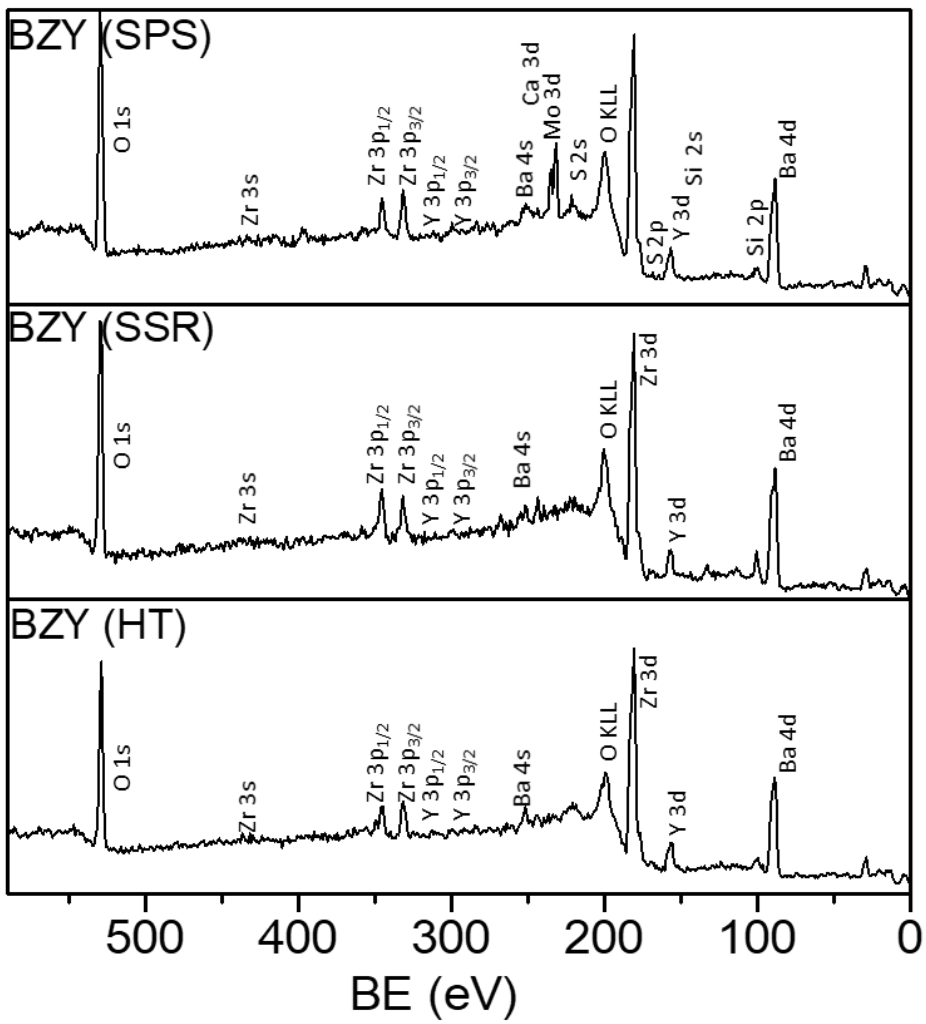

Figure 5: AP-XPS wide scan elemental survey spectra collected with photon energy of 710 eV under 100 mTorr of Ar at 500 °C for the SPS, the SSR and the HT samples.

3.2.2. Changes in O 1s and Y 3d with temperature and atmosphere

Similarly to previous studies on thin films [26], the Ba 4d and Zr 3d peaks do not change with temperature and atmosphere (Figures 3 SI, 4 SI, and 5 SI). This indicates that Ba and Zr are not redox active during changes in oxygen partial pressures P_{O2}. On the other hand, changes in the Y 3d core-level spectra were reported on BZY10 thin films, where the hydration is associated with oxygen under coordinated yttrium and/or yttrium hydroxide. This phenomenon is not observed on the three BZY samples in this study: two doublets are observed for the Y 3d core level spectra (157.3±0.2 and 155.7±0.2 eV for $3d_{5/2}$), corresponding to hydroxide surface species (main contribution) and lattice contribution (Figures 3 SI - 6 SI). Similar Y 3d core level spectra are observed for the three samples, with no clear difference in the Y 3d doublets with changing the atmosphere (Figure 3 SI -5 SI) or the beam energy (Figure 6 SI). A plausible explanation is that even under dry environment at high temperature, hydroxyl group remains at near surface yttrium sites (IMFP Y 3d ~ 2 nm). Physisorbed water may be progressively transformed into strongly adsorbed species, and subsequent dissociation can lead to incorporation of hydroxides into the near surface/lattice, in the form of yttrium hydroxide. Proton-trapping has been previously observed in the vicinity of yttrium in presence of zirconium in barium perovskites [46,47,48,49]. This trapping effect may be enhanced by the presence of grain boundaries that can promote molecular water adsorption and subsequent formation of stable yttrium hydroxide species near the surface. Yttrium segregates to BZY grain boundaries as shown in Table 2 and in previous studies [36-38,41]. This results in yttrium bulk deficiency but increased presence of hydroxides in the grain boundaries. Estimation of the B-site stoichiometry for the three samples that was performed using the 490 eV data for Y and 710 eV data for Zr (corresponding to a similar depth), and the results in Table 3 highlight the sub-stoichiometric amounts of yttrium in the near surface regions.

Table 3: B-site stoichiometry from AP-XPS data using 490 eV data for Y (IMFP~12.5Å) and 710 eV data for Zr (IMFP~13.9Å):

Sample	Expected	SPS	SSR	HT
Zr on B-site	0.90	0.92 (±0.05)	0.95 (±0.05)	0.92 (±0.05)
Y on B-site	0.10	0.08 (±0.01)	0.05 (±0.01)	0.08((±0.01)

Figure 6 compares the O 1s peak for the three samples at a photon energy of 710 eV for each of the gas compositions at 500 °C. Based on previous references [50,51,52,53], the O 1s peak can be deconvoluted into four contributions [26]:

1) low binding energy, ~528.6-529.1 eV: oxygen in the perovskite lattice structure, abbreviated as O^{2-},
2) medium binding energy at ~530-530.3 eV: under-coordinated oxygen in the surface termination layer associated with partially hydrated surface secondary phases and/or adsorbates,
3) high binding energy, at 531.5-532 eV: surface hydroxylation and molecular water adsorption (denoted "OH^{-}"),
4) highest binding energy, at ~533.5- 534 eV: Water vapor at the surface (denoted "steam") [54].

"Regarding the OH^{-} contribution, a minimal contribution for all three samples is observed under argon at 500 °C. The small OH^{-} signal suggests residual hydration from the sample preparation in ambient air. Under 100 mTorr H_2O at 300 °C, the OH^{-} contribution is significantly larger and its intensity decreases with increasing the temperature to 500 °C. This is due to the exothermicity of the hydration reaction that leads to a drop in the concentration of protonic defects with increasing the temperature[1,7]. After the treatment for 2.5 hours in oxygen at 500 °C, the sample is almost fully dehydrated, with an OH^{-} contribution similar to the one observed under argon at 500 °C.

For the lattice O^{2-} contribution, by comparison with the OH^{-}, for all samples, the contribution follows the expected inverse tendency, being maximal at 500 °C under argon and oxygen, and minimal in humid atmosphere, where the samples are hydrated. One should notice that the lattice O^{2-} signal is however significantly smaller under oxygen than under argon. This is another indication that the hydration process might be accompanied by a surface degradation process leading to the formation of secondary phases. This hypothesis is reinforced by the behavior of the medium binding energy component that gradually increases, from under argon at 500 °C to humid environment at 300 °C and then at 500 °C, while decreasing but remaining high under oxygen at 500 °C. This indicates that the medium binding energy contribution is most likely associated with secondary phases formation rather than oxygen vacancies/under-coordinated

oxygen at the surface. As no significant changes in the Ba, Zr, Y stoichiometry ratio or XPS core-level spectra were observed under the different environments, the correlation with the Ba/Y grain boundaries segregation effects was not apparent.

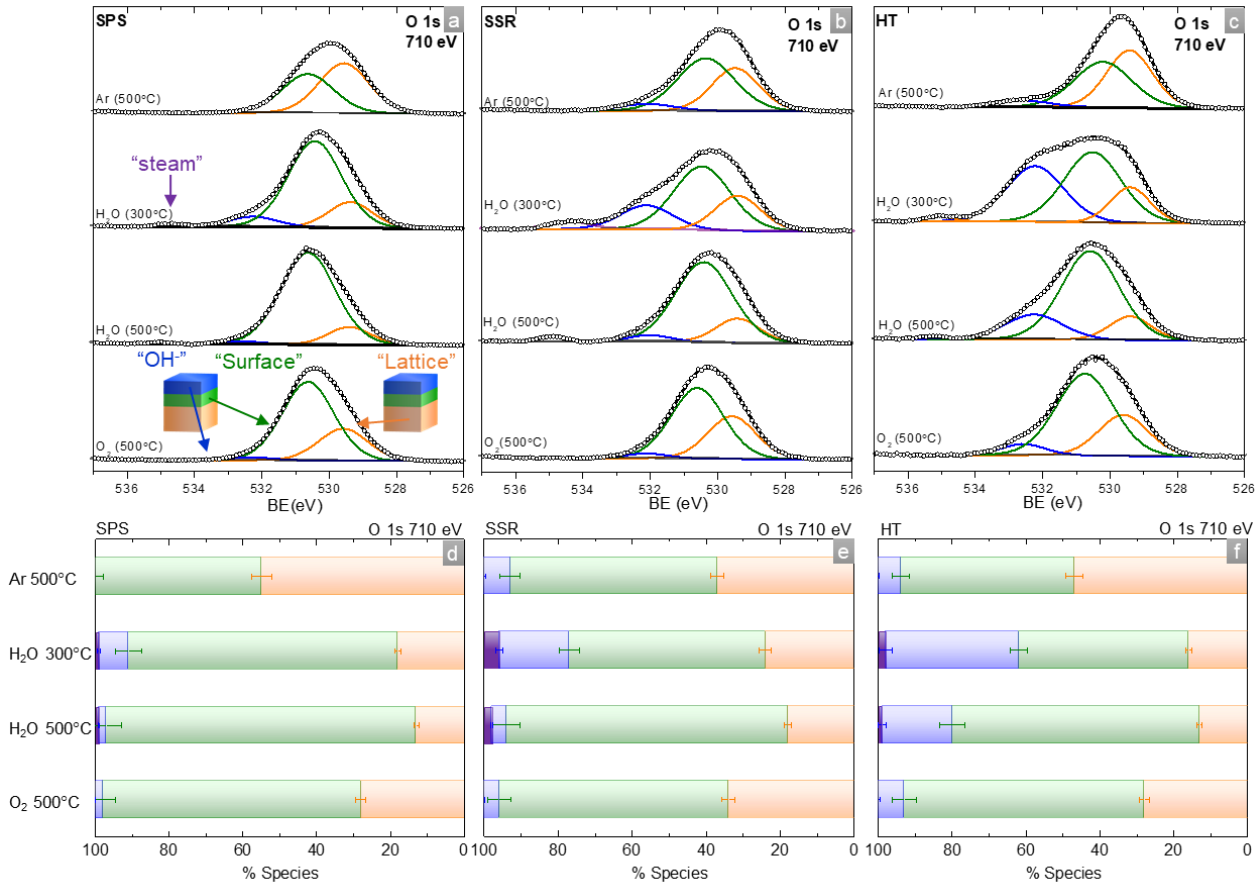

Figure 6*:* O 1s *In situ* AP-XPS spectra of the $BaZr_{0.9}Y_{0.1}O_{3-\delta}$ (a) SPS, (b) SSR and (c) HT pellets with incident X-ray energy of 710 eV as a function of environment (100 mTorr of Ar, H_2O or O_2) and temperature (300 °C and 500 °C). The "lattice" component shown in orange represents the perovskite structure in the near surface regions while the "surface" component shown in green is for partially hydrated surface secondary phases with "OH^-" corresponding to the hydration/adsorbed species (blue). The "steam" component is represented in purple. White circles represent the measured data, black lines correspond to the sum of fits, and grey lines are for the background. (d), (e) and (f) represent the variation in the relative contributions of "lattice", "surface", "OH^-" and "steam" components to the total O 1s. Error bars are estimated using Monte Carlo simulations as the 95% confidence intervals [52].

The O 1s spectra for the three samples at 300 °C under steam (maximal hydration) presented in Figure 7 were collected using three different photon energies. With increasing photon energy,

the relative contribution of the "lattice" increases while the two other contributions decrease. This is in line with our previous work [26] where the hydroxylation was also more important at the very surface of the samples. This is also in agreement with the hypothesis of surface secondary phase formation (green contribution) under moist environments.

The use of 'hydroxylation' instead of 'hydration' indicates the hypothesis that the OH^- contribution arises only in part from protonic defects incorporated into the lattice (Reaction 1). Even for a fully hydrated sample, the observed OH^- contribution to the O 1s is far too large considering the 1.5 % of intrinsic oxygen vacancies of the bulk $BaZr_{0.9}Y_{0.1}O_{3-\delta}$. A plausible explanation for this excess resides in the peak overlaps between the species present at the $BaZr_{0.9}Y_{0.1}O_{3-\delta}$ surface. Yttrium hydroxide is formed from water molecules adsorbed at the BZY10 surface. The O1s binding energies corresponding to hydroxylation, adsorbed molecular water or hydration cannot be distinguished in our spectra. To simplify the notation these three different species are comprised in the "OH^- "contribution.

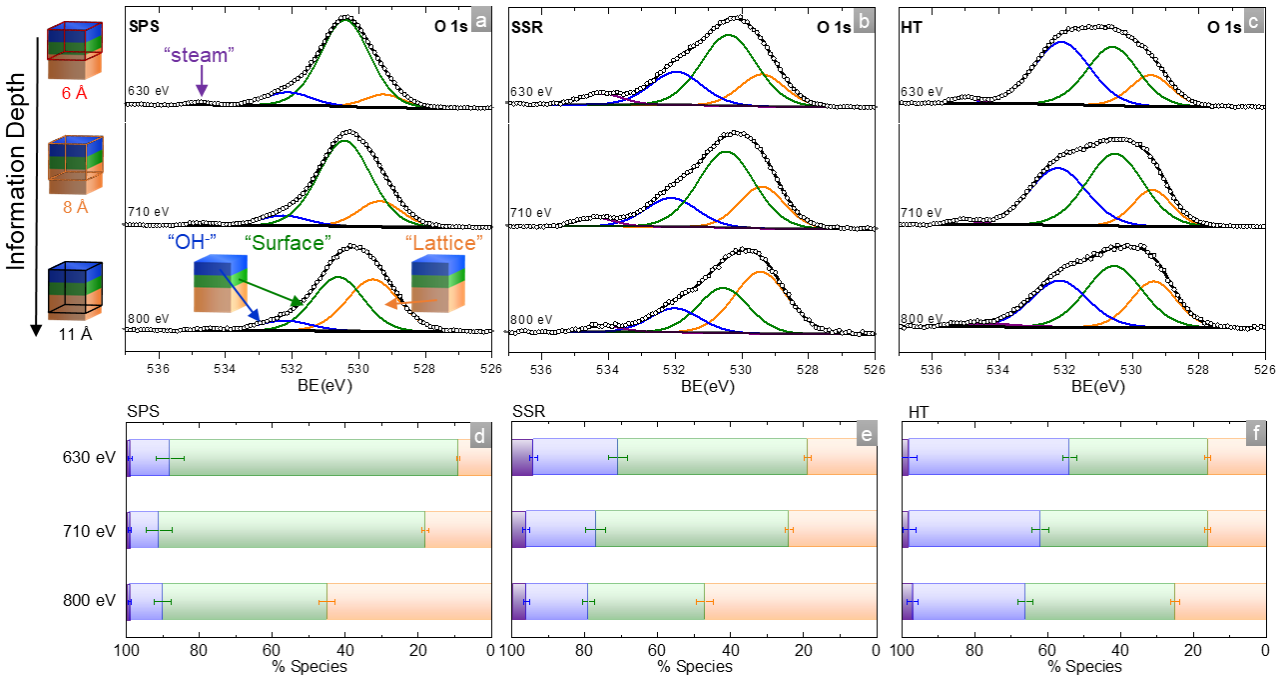

Figure 7: O 1s *in situ* AP-XPS spectra of the $BaZr_{0.9}Y_{0.1}O_{3-\delta}$ (a) SPS, (b) SSR and (c) HT pellets as a function of the incident X-ray energy (630 eV, 710 eV, 800 eV) at 300 °C at a $p(H_2O)$ of 100 mTorr. The collection of O 1s at three different photon energies provides information from the surface to higher depth into the samples, 6 Å, 8 Å and 11 Å respectively, according to the IMFP calculation for O 1s. The "lattice" component shown in orange represents the perovskite

structure in the near-surface regions while the "surface" component shown in green is for partially hydrated surface secondary phases with "OH^-" corresponding to the hydration/adsorbed species (blue). The "steam" component is represented in purple. White circles represent the measured data, black lines correspond to the sum of fits, and grey lines are for the background. (d), (e) and (f) represent the variations in the relative contributions of "lattice", "surface", "OH^-" and "steam" components to the total O 1s. Error bars are estimated using Monte Carlo simulations as the 95% confidence intervals [52].

4. Discussion

The above results show that the hydroxylation contribution increases from the SPS to the SSR and finally to the HT sample. This phenomenon can potentially be explained by a variety of phenomena such as changes in one or more of the following:

1) chemical composition of the grain interiors and/or boundaries,
2) sample histories,
3) grain sizes and morphologies of the surface.

Regarding the first hypothesis, former chemical analyses performed on the HT and SPS samples[45] confirm similar grain interior/grain boundary composition ratios between the two samples (see Table 2), with barium and yttrium segregation and zirconium and oxygen depletion at the grain boundaries. Despite the similar chemical compositions, the HT sample exhibits significantly higher hydroxylation than the SPS sample. This allows us to conclude that a bulk chemical variation between samples cannot be at the origin of the effect we observed with AP-XPS.

All samples were polished and pre-heated/dehydrated following the same procedure before the AP-XPS experiments (inside the analysis chamber, 500 °C, ultra-high vacuum for several hours). We assume that the samples surface compositions were modified evenly. This rules out sample history/surface termination as a possible cause for the phenomenon we observed.

The SEM images (Figure 4) highlight that the grain size and surface morphology of each sample is distinct. These differences appear to correlate with variations in the O 1s. Table 4 summarizes the percentage of the hydroxyl contribution to the total O 1s area as a function of the average grain size (0.3-0.8, 1 and 2-5 microns for the SPS, SSR and HT samples respectively),

for the different beam energies in steam at 300 °C. It is clear that the hydroxylation contribution increases with grain size and is larger at the surface compare to the near surface/lattice (lower beam energy/IMFP).

Table 4: Percentage of the OH^- contribution to the total O 1s area in steam at 300 °C as a function of the average grain size: 0.3-0.8, 1 and 2-5 microns for the SPS, SSR and HT samples respectively.

Grain size	% OH^- contribution (IMFP ~ 6 Å)	% OH^- contribution (IMFP ~8 Å)	% OH^- contribution (IMFP~11 Å)
0.3-0.8 μm	10.8	7.8	8.9
1 μm	22.7	18.7	17.2
2-5 μm	44	36.3	31.3

Thus, it appears that hydration due to water adsorption and incorporation is favored in the sample with the larger grains. Even though the synthesis methods between thin films and pellets are very different and result in different termination layers, a grain-boundary-free epitaxial thin film can be essentially considered has an infinite grain with very low surface roughness. In our previous study on such epitaxial BZY10 thin film[26], the OH^- contribution of hydration was no more than 7% at an IMFP of 8 Å. Thus, we cannot ascribe the hydroxylation contribution increase to the grain size alone. As discussed earlier, the main difference between the samples studied here is their grain size and associated grain boundaries and surface morphology. Therefore our hypothesis is that the grain-boundaries/surface morphology for larger grains favor hydroxylation via molecular water adsorption, as illustrated in Figure 8. It was already mentioned that the yttrium segregates to the grain boundaries as reported in Table 2 and previous studies [36-38,41]. In this work, we demonstrate that this segregation results in the formation of a high amount of stable yttrium hydroxides that effectively trap the protons. In addition, the gaseous contribution of steam (534-535 eV) is observed on the three studied BZY samples (see purple contribution in Figures 6 and 7), which was not the case for the thin films [26]. This gaseous contribution must be connected to the presence of grain-boundaries/higher roughness of

the surface. These two observations are in agreement with the sketch presented in Figure 8.

Impedance spectroscopy measurements[43] revealed very similar bulk conductivities for the samples while the larger grain one exhibited higher protonic conductivity across the grain boundary and overall better performance. It is assumed that larger grains enhance conductivity of BZY because space-large layers at grain boundaries inhibit ionic transport and thus increase resistivity [43]. As this study highlights, there is a clear affinity for grain boundaries of larger grains to adsorb water and form OH^- near the surface. This increased water adsorption and OH^- formation may positively impact conductivity/performance by enhancing the resistance of an electrode to surface carbon build-up. Indeed, it was shown that Ni-BZY anodes are significantly less prone to coking than Ni-YSZ in the presence of methane and water steam[4]. In this work, a mechanism for coke removal in BZY fuel cell operation suggested that high levels of OH^- adsorption on the BZY surface encouraged formation of COOH on the Ni nanoparticles (COOH (Ni)) to mitigate coke formation, hence, resulting in a significant improvement of the fuel cell operation performance. The present study is in line with that work and suggests that larger grains may be beneficial not only by improving the conductivity level but also by promoting surface carbon removal. We propose that this unique combination of effects is at the origin of the exceptional performance of the larger BZY grains.

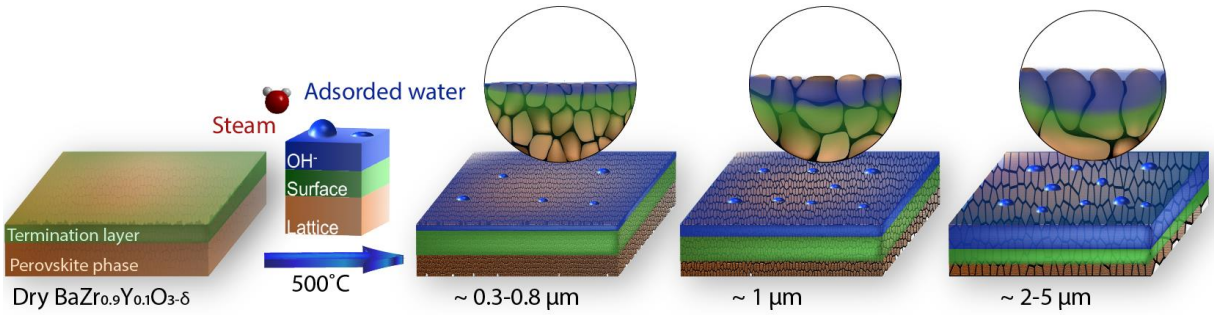

Figure 8: Schematic representations of the grain size effects on barium perovskites $BaZr_{0.9}Y_{0.1}O_{3-\delta}$ surface chemistry. The "lattice" component for the perovskite structure in the near surface regions is shown in brown orange while the "surface" component for partially hydrated surface secondary phases on the pellet is shown in green with the blue corresponding to the hydration/water adsorption. At temperature, under partial pressure of water, larger grains favor hydration via filling of the oxygen vacancies and adsorption of water at the surface.

4. Conclusions

Ambient-pressure X-ray photoelectron spectroscopy was used at Beamline 9.3.2 at the Advanced Light Source to correlate the extent of near-surface hydration with the grain size and associated grain boundaries. Three $BaZr_{0.9}Y_{0.1}O_{3-\delta}$ (BZY10) pellets were prepared using different sintering processes: spark plasma sintering, solid state reaction followed with conventional sintering, with and without a final high temperature annealing step. The grain size of the samples ranges from 0.3 to 5 microns. AP-XPS spectra were recorded in argon, steam and oxygen atmospheres (100 mTorr) at 300 °C and 500 °C. The analysis of the O 1s peak in the different gas atmospheres and two temperatures gave two significant insights: the OH^- contribution is found to increase with increasing the grain size, and to decrease with increasing the analysis depth.

Previous work focused on the chemical composition and conductivity measurements of two of the present samples: SPS and HT.[42] Very similar bulk values were obtained for the samples while the larger grains exhibits higher protonic conductivity across the grain boundary [43]. This confirms that the change in hydroxylation between the samples seems to be related mainly to the grain size and associated grain boundaries. The hypothesis proposed to explain this observation is that grain boundaries for the larger grains facilitate adsorption of molecular water, based on the presence of gaseous steam and higher OH^- contribution to the O 1s.

Conflicts of interest:

There are no conflicts of interest to declare.

Acknowledgments:

This work was supported by the Colorado School of Mines Foundation via the Angel Research Fund, the Office of Naval Research (ONR) and The Advanced Light Source (ALS) funded by the U.S. Department of Energy, Office of Science, and Office of Basic Energy Sciences under award DESC0001160 and Contract No. DE-AC02-05CH11231 respectively.

References:

[1] K.D. Kreuer, *Annu Rev Mater Res*, 2003, **33**, 333.

[2] E. Fabbri, D. Pergolesi, E. Traversa, *Chem Soc Rev*, 2010, **39**, 4355.

[3] A. Løken, S. Ricote, S. Wachowski, *Crystals*, 2018, **8**, 365.

[4] C. Duan, R.J. Kee, H. Zhu, C. Karakaya, Y. Chen, S. Ricote, A. Jarry, E. Crumlin, D. Hook, R. Braun, N.P. Sullivan, R. O'Hayre, *Nature*, 2018, **557**, 217.

[5] N. Bonanos, *Solid State Ionics*, 1992, **53-56**, 967.

[6] F.W. Poulsen, *J. Solid State Chem*, 1999, **143**, 115.

[7] S. Ricote, N. Bonanos and G. Caboche, *Solid State Ionics*, 2009, **180**, 990.

[8] H. Zhu, S. Ricote, C. Duan, R.P. O'Hayre, D.S. Tsvetkov, R.J. Kee, *J Electrochem Soc*, 2018, **165**, F581.

[9] S. Ricote, N. Bonanos, M.C. Marco De Luca, G. Caboche, *J Power Sources*, 2009, **193**, 189.

[10] D. Han, Y. Noda, T. Onishi, N. Hatada, M. Majima, T. Uda, *Intern J Hydrogen Energy*, 2016, **41**, 14897.

[11] V.S. Stotz, C. Wagner C, *Ber Bunsenges Phys Chem*, 1960, **70**, 781.

[12] T. Norby, Y. Larring, *Current Opinion in Solid State & Materials Science*, 1997, **2**, 593.

[13] T. Schober, W. Schilling, H. Wenzl, *Solid State Ionics*, 1996, **86-88**, 653.

[14] T. Schober, H.G. Bohn, *Solid State Ionics*, 2000, **127**, 351.

[15] C. Kjølseth, L.-Y. Wan, R. Haugsrud, T. Norby, *Solid State Ionics*, 2010, **151**, 1740.

[16] D. Han, K. Shinoda, T. Uda, *J Am Ceram Soc*, 2014, **97**, 643.

[17] E. Fabbri , D. Pergolesi, S. Licoccia, E. Traversa, *Solid State Ionics*, 2010, **181**, 1043.

[18] C. Hiraiwa, D. Han, A. Kuramitsu, A. Kuwabara, H. Takeuchi, M. Majima, T. Uda, *J Am Ceram Soc*, 2013, 96, 879.

[19] A.K.E. Andersson, S.M. Selbach, C.S. Knee, T. Grande, *J Am Ceram Soc*, 2014, **97**, 2654.

[20] R. Sazinas, M.-A. Einarsrud, T. Grande, *J Mater Chem A*, 2017, **5**, 5846.

[21] G. Hudish, A. Manerbino, W.G. Coors, S. Ricote, *J Am Ceram Soc, 2018*, **101**, 298.

[22] Y. Yamazaki, F. Blanc, Y. Okuyama, L. Buannic, J.C. Lucio-Vega, C.P. Grey, S.M. Haile, *Nature Materials*, 2013, **12**, 647.

[23] P. Berger, A. Sayir, M.-H. Berger, 28th International Conference on Advanced Ceramics and Composites A: Ceramic Engineering and Science Proceedings, Volume 25, Issue 3 (eds E. Lara-Curzio and M. J. Readey), John Wiley & Sons, Inc., Hoboken, NJ, USA.

[24] A. Slodczyk, P. Colomban, S. Willemin, O. Lacroix, B. Sala, *J Raman Spectrosc*, 2009, **40**, 513.

[25] Q. Chen, F. El Gabaly, F. Aksoy Akgul, Z. Liu, B.S. Mun, S. Yamaguchi, A. Braun, *Chem Materials*, 2013, **25**, 4690.

[26] A. Jarry, S. Ricote, A. Geller, C. Pellegrinelli, X. Zhang, D. Stewart, I. Takeuchi, E. Wachsman, E.J. Crumlin, B. Eichhorn, *ACS Applied Materials & Interfaces*, 2018, **10**, 37661.

[27] S. Axnanda, E.J. Crumlin, B. Mao, S. Rani, R. Chang, P.G. Karlsson, M.O.M. Edwards, M. Lundqvist, R. Moberg, P. Ross, Z. Hussain, Z. Liu, *Scientific Reports*, 2015, **5**, 9788.

[28] F.M.M. Snijkers, A. Buekenhoudt, J. Cooymans, J.J. Luyten, *Scr Mater*, 2004, **50**, 655.

[29] P. Babilo, T. Uda and S. M. Haile, *J Mater Res*, 2007, **22**, 1322.

[30] F. Iguchi, N. Sata, T. Tsurui, H. Yugami, *Solid State Ionics*, 2007, **178**, 691.

[31] W.D. Kingery, *J Am Ceram Soc*, 1974, **57**, 74.

[32] M.F. Yan, R.M. Cannon, H.K. Bowen, *J Appl Phys*, 1983, **54**, 764.

[33] S.B. Desu, D.A.J. Payne, *Am Ceram Soc* 1990, **73**, 3398.

[34] M. Shirpour, B. Rahmati, W. Sigle, P.A. van Aken, R. Merkle, J. Maier, *J Phys Chem C* 2012, **116**, 2453.

[35] A.K. Azad, C. Savaniu, S. Tao, S. Duval, P. Holtappels, R.M. Ibberson, J.T.S. Irvine, *J Mater Chem*, 2008, **18**, 3414.

[36] C. Kjølseth, H. Fjeld, Ø. Prytz, P.I. Dahl, C. Estournes, R. Haugsrud, T. Norby, *Solid State Ionics*, 2010, **181**, 268.

[37] M. Shirpour, R. Merkle, C.T. Lin, J. Maier, *J Phys Chem Chem Phys*, 2012, **14**, 730.

[38] M. Shirpour, R. Merkle, J. Maier, *Solid State Ionics*, 2012, **216**, 1.

[39] J.-S. Kim, J.-H. Yang, B.-K . Kim, Y.-C. Kim, *Solid State Ionics*, 2015, **275**, 19.

[40] A. Lindman, E.E. Helgee, G. Wahnström, *Solid State Ionics* 2013, **252**, 121.

[41] S. Ricote, N. Bonanos, H. J. Wang and B. A. Boukamp, *Solid State Ionics*, 2012, **213**, 36.

[42] S.B.C. Duval, P. Holtappels, U.F. Vogt, E. Pomjakushina, K. Conder, U. Stimming, T. Graule, *Solid State Ionics*, 2007, **178**, 1437.

[43] S. Ricote, N. Bonanos, A. Manerbino, N. P. Sullivan, W. G. Coors, *J Mater Chem A*, 2014, **2**, 16107.

[44] M.E. Grass, P.G. Karlsson, F. Aksoy, M. Lundqvist, B. Wannberg, B.S. Mun, Z. Hussain, Z. Liu, *Rev Sci Instrum*. 2010, **81**, 053106.

[45] D. R. Clark, Ph.D. thesis, 2015, Colorado School of Mines.

[46] R. Hempehnann, C. Karmonik, T. Matzke, M. Cappadonia, U. Stimming, T. Springer, M.A. Adams, *Solid State Ionics*, 1995**, 77**, 152.

[47] R. Hempelmann, M. Soetratmo, O. Hartmann, R. Wäppling, *Solid State Ionics*, 1998, **107**, 269.

[48] M.E. Bjorketun, P.G. Sundell, G. Wahnstrom, *Faraday Discussions*, 2007, **134**, 247.

[49] R. Glöckner, M.S. Islam, T. Norby, *Solid State Ionics*, 1999, **122**, 145

[50] E.J. Crumlin, E. Mutoro, W.T. Hong, M.D. Biegalski, H.M. Christen, Z. Liu, H. Bluhm, Y. Shao-Horn, *J Phys Chem C*, 2013, **117**, 16087.

[51] E. Mutoro, E.J. Crumlin, M.D. Biegalski, H.M. Christen, Y. Shao-Horn, *Energy & Environmental Science*, 2011, **4**, 3689.

[52] K.A. Stoerzinger, W.T. Hong, E.J. Crumlin, H. Bluhm, M.D. Biegalski, Y. Shao-Horn, *J Phys Chem C*, 2014, **118**, 19733.

[53] E.J. Crumlin, E. Mutoro, Z. Liu, M.E. Grass, M.D. Biegalski, Y.-L. Lee, D. Morgan, H.M. Christen, H. Bluhm, Y. Shao-Horn, *Energy & Environmental Science*, 2012, **5**, 6081.

[54] S. Yamamoto, H. Bluhm, K. Andersson, G. Ketteler, H. Ogasawara, M. Salmeron, A. Nilsson, *J Physics: Condensed Matter*, 2008, 20, 184025.
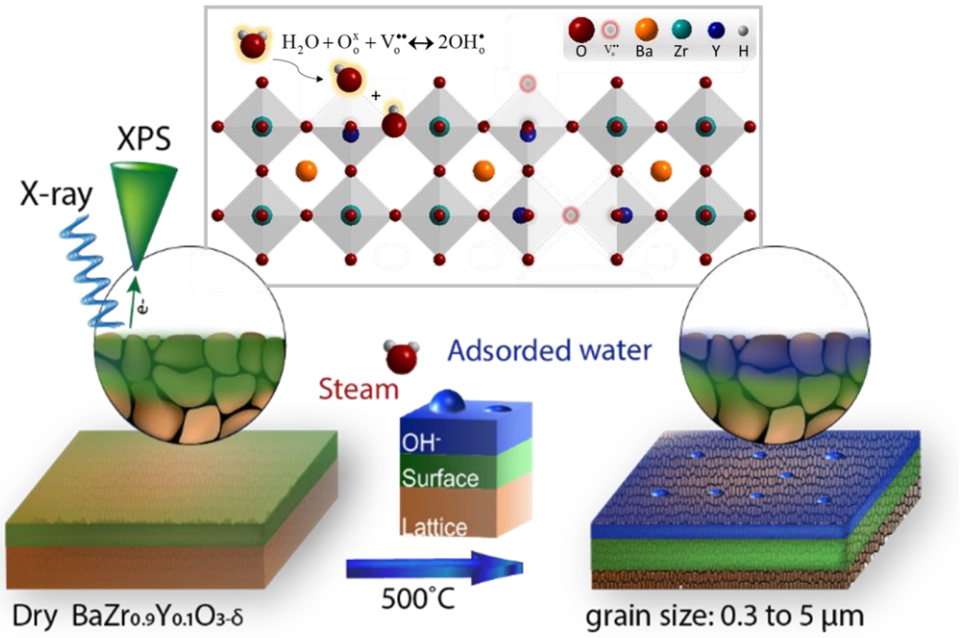
Graphical abstract